

Measurement of weak Zeeman effect in mercury (Hg I) atoms and the $H\alpha$ spectral lines of (^1H) Protium and (^2H) Deuterium

Ryan Mok, Rishi Brar, and Danae Kalyva
University College London
Department of Physics and Astronomy

8th January 2024

Word Count: 2450 (Excl. appendix, reference etc.)

Abstract

We measure the weak Zeeman effect in neutral mercury Hg(I) atoms subjugated to a magnetic field of 1.5 ± 0.1 T and the H α Balmer series line for a hydrogen lamp consisting of isotopes protium (^1H) and deuterium (^2H). Images of spectral lines are captured with a CCD camera and converted into spectral line intensity distributions. Analysis shows that the observed weak Zeeman effect on neutral mercury atoms is consistent with the qualitative predictions formed by quantum mechanics. The wavelength shifts between H α lines of protium and deuterium allow calculations of the proton-deuteron mass ratio. Least-square Gaussians are fitted onto H α intensity distributions to extract values of the wavelength shifts. This yields a proton-deuteron mass ratio of 0.51 ± 0.02 , in agreement and within 1.95% error of the accepted value of 0.5002.

1 Introduction and Theory

This experiment consists of two parts. We first qualitatively measure the weak Zeeman effect in neutral Mercury atoms with an external magnetic field of 1.5 ± 0.1 T. The second part measures the H-alpha (H α) lines for protium and deuterium which allows a calculation of the proton-deuteron mass ratio. We start with an overview of theory behind the experiment.

(Weak) Zeeman Effect in Mercury:

Zeeman effect is a quantum phenomenon of spectral lines from a source splitting as a result of subjugating the source to an external magnetic field. It is explained by perturbative shifts of the external magnetic field on energy levels of the source. Within physics, Zeeman effect has wide applications in spectroscopy. For instance, measurements of magnetic fields in high temperature plasmas can be done through spectroscopy with the Zeeman effect, which removes the use of equipment such as probes which can be damaged and distort the magnetic field [8].

This experiment measures three different spectral lines of mercury described below:

Transition States ($^{2S+1}L_J$ Terms)	Wavelength(nm)	Colour
$(6s6d) \ ^1D_2 \rightarrow (6s6p) \ ^1P_1$	579.0670 ± 0.0001	‘Yellow’
$(6s7s) \ ^3S_1 \rightarrow (6s6p) \ ^3P_2$	546.0750 ± 0.0001	‘Green’
$(6s7s) \ ^3S_1 \rightarrow (6s6p) \ ^3P_1$	435.8335 ± 0.0001	‘Blue’

Table 1: Spectral lines of Hg(I) which will be measured. Data obtained from NIST[7].

When mercury atoms are placed into an external magnetic field, the energy levels of quantum states are perturbatively shifted by

$$\Delta E = \mu_B g_J B_{ext} M_J \quad (1)$$

This works under the assumption that spin-orbit coupling perturbations are much larger, which defines the ‘weak Zeeman effect’ [2]. μ_B is a constant named the ‘Bohr magneton’. B_{ext} is the external magnetic field, M_J is the quantum number related to operator \hat{J}_z . g_J is the ‘Lande g-factor’, dependent on quantum numbers L, S, J.

The perturbation breaks the degeneracy of m_J which leads to the splitting of transition lines. Under transition selection rules ($\Delta m_J = 0, \pm 1$ and for $\Delta J = 0, \Delta m_J \neq 0$), the ‘yellow’ spectral line splits into three lines whilst ‘blue’ and ‘green’ lines split into six and nine spectral lines respectively. Our objective is to verify this prediction.

Hydrogen H α Line and Proton-Deuteron mass ratio:

The H α line of hydrogen consists of red wavelength transitions from quantum state $(3s) {}^2S_{1/2}$ to either the state $(2p) {}^2P_{1/2}$ or $(2p) {}^2P_{3/2}$. It has become ubiquitously used within the techniques of astronomy. One of its many applications is to study star formation in galaxies. By looking at the width and intensity of the H α emission line, one may obtain a prediction for the star formation rate in galaxies [13].

Protium refers to the isotope of hydrogen with a nucleus of one proton. Deuterium refers to the isotope of hydrogen with a deuteron (proton and neutron) nucleus. A relation can be derived (Appendix A) between the proton-deuteron mass ratio and the difference in wavelength between the protium H α line and deuterium H α line. Namely,

$$\frac{M_P}{M_D} = 1 - \left(1 + \frac{M_P}{m_e}\right) \left[\frac{\lambda_P - \lambda_D}{\lambda_P}\right] \quad (2)$$

M_P , M_D are the proton, deuteron masses while λ_P , λ_D is the wavelength of the H α line for protium, deuterium respectively. m_e is the electron mass. The H α line is further complicated by fine-structure perturbations from spin-orbit coupling and relativistic corrections. This removes degeneracy in quantum number J splitting the two transitions which comprise the initially one H α line into two separate lines.

There is a second complication from $H\alpha$ spectral lines being Doppler broadened. This is caused by hydrogen atoms moving with velocities parallel to the direction of photon emission causing a Doppler shift. The importance of this is explained in analysis. Fine structure and broadening features can be shown as an intensity-wavelength graph in Fig. 1.

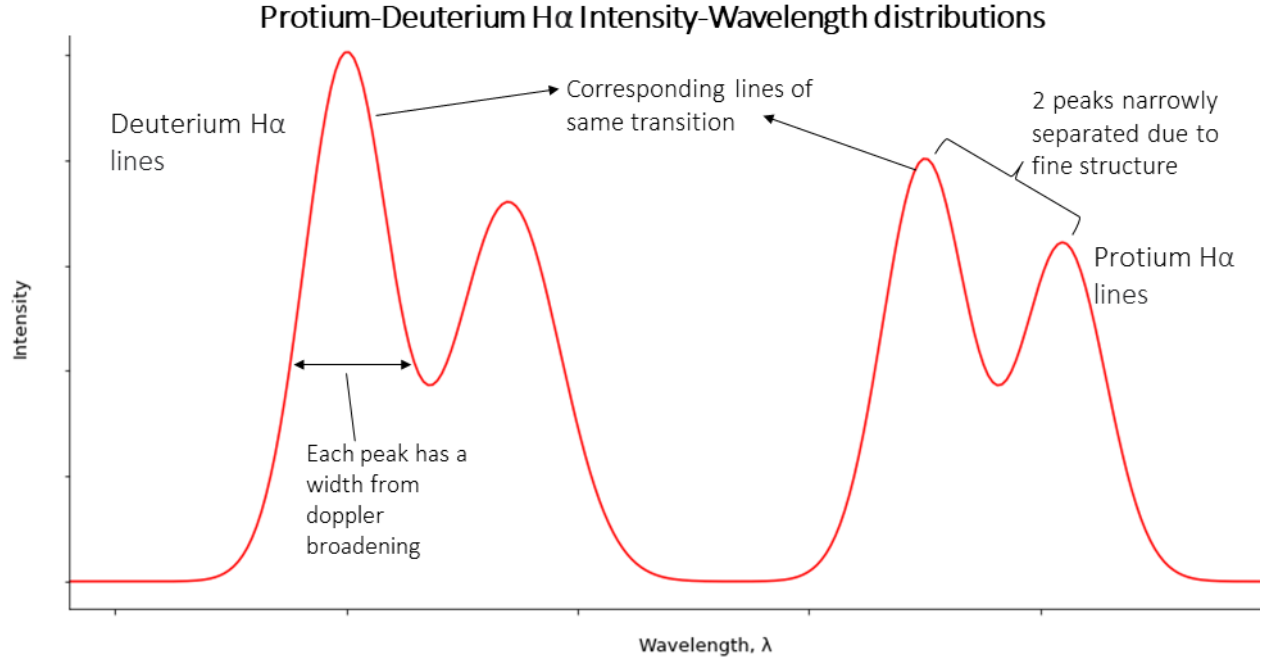


Figure 1: The $H\alpha$ emission distribution line for source of protium and deuterium [9]. Relative intensities of protium and deuterium lines are dependent on their relative abundance in the source. Intensities in the fine structure peaks differ due to different transition probabilities.

Provided we can measure the difference in wavelength between the correct corresponding transitions of $H\alpha$ lines in protium and deuterium, we may calculate the proton-deuteron mass ratio since other constants are well known. This is the objective of the second part of the experiment.

2 Experimental Methodology

The main apparatus consists of mercury lamp (Spectroline 11SC-1 OP) slotted between poles of an electromagnet, a hydrogen lamp composed of protium and deuterium and a spectrometer setup. The spectrometer is based on Czerny-Turner configurations, which includes an input slit with a collimating mirror, plane mirror and echelle diffraction grating, allowing higher resolution power [6].

The spectral lines which pass through the spectrometer are output onto a CCD camera which ultimately forms an image of the spectral lines. We use a software called 'ImageJ' to form spectral

intensity distributions. ImageJ takes a horizontal cross section of our image and forms datapoints of the horizontal-pixel value and the greyscale value of the corresponding image pixel. We then normalize greyscale values to obtain a relative intensity distribution of the emission spectra with respect to horizontal-pixel values.

In order to obtain wavelength width ($\lambda_P - \lambda_D$), it can be shown that using the diffraction grating (Appendix B), change in wavelength and a change in horizontal-pixel value is related by

$$\Delta\lambda = \frac{\lambda_P}{1.150 \times 10^6} \Delta x \quad (3)$$

Where the change in wavelength ($\Delta\lambda$) is given in nanometers(nm) and Δx is the change in pixel-value. Therefore, we may find pixel width by taking the change in the pixel-values of the peaks of corresponding line transitions in protium and deuterium from our intensity distributions. By Eq. 3 we are then able to therefore find the value of the wavelength width. Subsequently, this method therefore allows us to calculate the proton-deuteron mass ratio through Eq. 2.

Experimental Procedure:

The first part of experimental procedure involves alignment of the spectrometer. Before viewing spectra, a laser (Thorlabs KM100) is used to ensure that light input follows the beam path as seen in Fig 2.

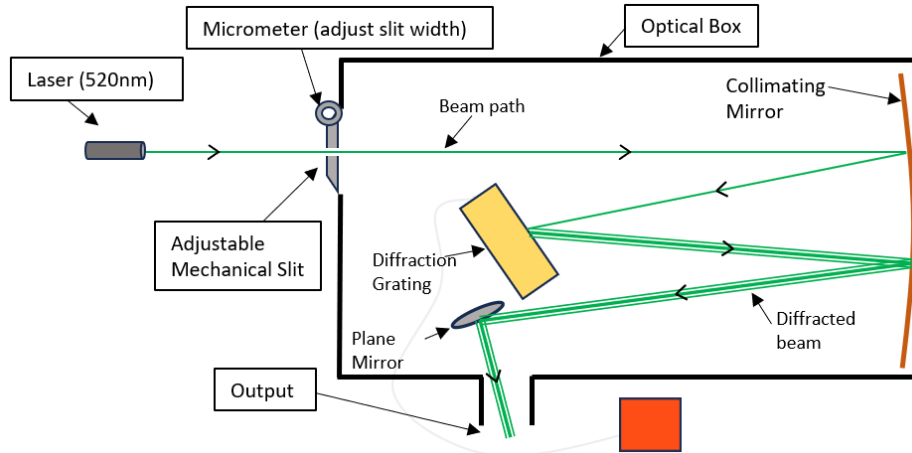


Figure 2: Apparatus schematic during laser alignment of the spectrometer.

Several components of the spectrometer are adjusted. The micrometer is turned such that the slit is sufficiently large and the beam passes through the slit into the optical box. The laser position and orientation is modified to allow the beam into the optical box if required. The diffraction grating and plane mirror are turned (manually) until a diffraction pattern is centered on the collimating

mirror and plane mirror. Alignment was complete when paper is placed at the output and a clear interference pattern is projected on the paper.

The second step of the procedure focuses on viewing line spectra in both Zeeman effect of mercury and protium-deuterium. The laser is removed and replaced with a focusing lens for Zeeman effect. For $H\alpha$ lines, we have the hydrogen lamp only (no focusing lens). An eyepiece lens is slotted into the spectrometer with the lamp turned on. The new setups are described in Fig. 3.1 and 3.2.

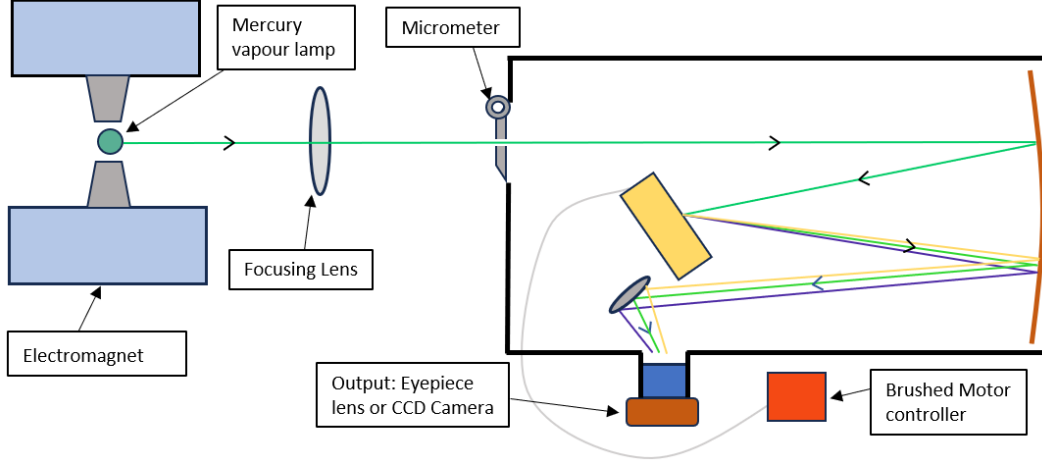


Figure 3.1: Apparatus schematic for measurement of Zeeman effect

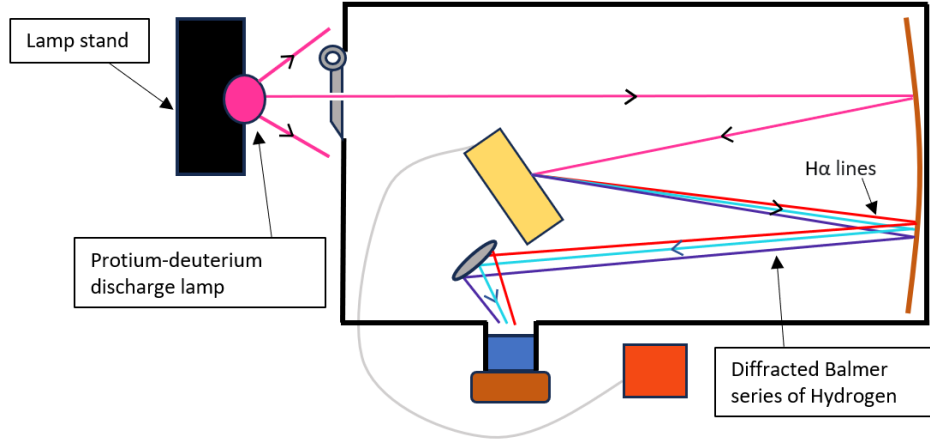


Figure 3.2: Apparatus schematic for measurement of $H\alpha$ spectra

A brushed motor controller (Thorlabs KDC101) finely rotates the diffraction grating to find and center different spectral lines through the eyepiece. Spectral lines are made sharp and as focused as possible through a series of small adjustments:

- The micrometer is turned until the slit is narrow as possible without comprising line brightness completely. The optimal micrometer value was between $0.100 \pm 0.005 \text{ mm}$ and $0.070 \pm 0.005 \text{ mm}$.
- For the Zeeman effect, focusing lens height and distance from slit are carefully adjusted. This is done with the electromagnet on and off.
- For $\text{H}\alpha$ spectra, we finely adjust the distance between the lamp and slit along with very slightly rotating the lamp.
- The eyepiece is adjusted in the slot to focus the image

Spectral lines are checked through the eyepiece. When quality of spectral lines are maximized, a CCD camera (ATIK ATK-314L+) is swapped with the eyepiece lens and images are taken with a 10 second exposure. For Zeeman effect, images are captured with the electromagnet on and off. Fine adjustments of the lens and micrometer are made whilst the camera is in place until image clarity is optimized. The best micrometer position is substantially smaller with the camera, reading values between $-0.050 \pm 0.005 \text{ mm}$ and $0.010 \pm 0.005 \text{ mm}$. Positioning of the camera itself must be adjusted to obtain focused images. For mercury, the procedure is repeated with each spectral line in Table 1.

3 Results

Zeeman effect in mercury:

Images taken by the CCD camera with the electromagnet on and off are shown below. We are able to see splitting in all three different lines.

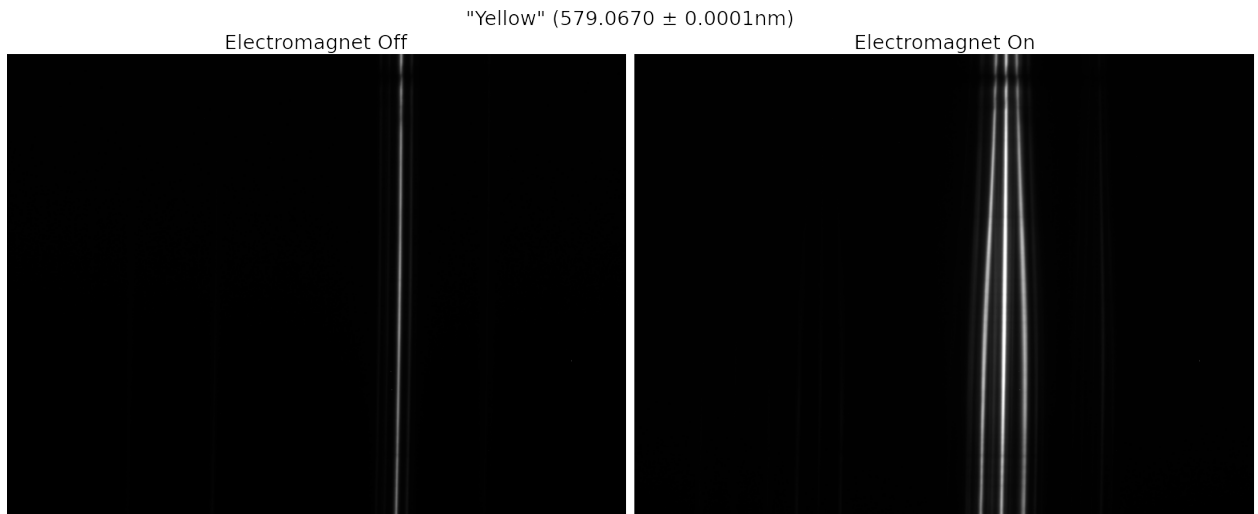


Figure 4.1: Zeeman splitting of the ‘yellow’ line.

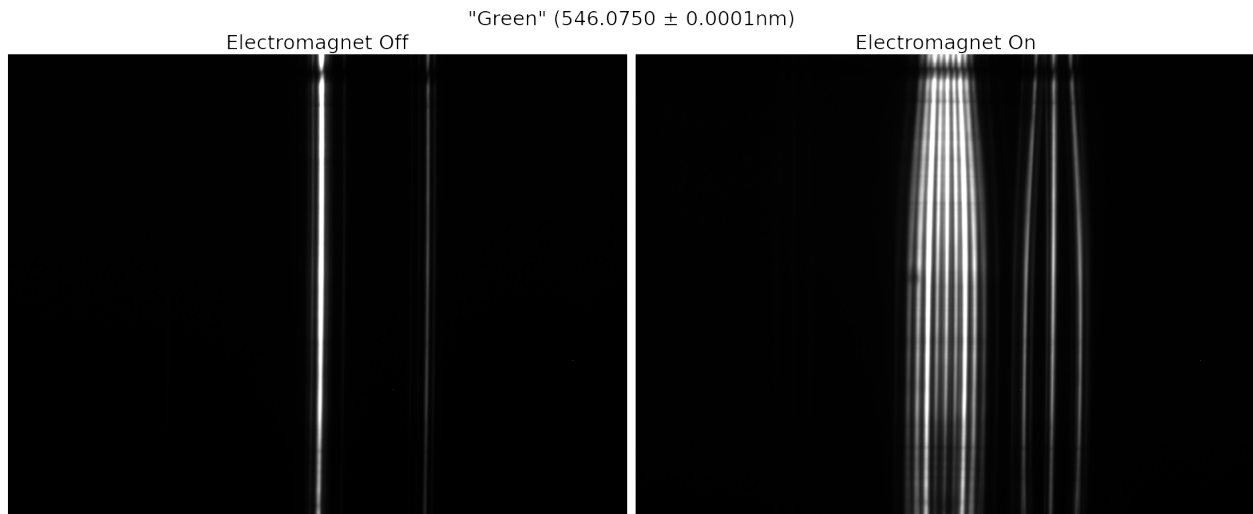


Figure 4.2: Zeeman splitting of the 'green' line. There is an overlapping 'yellow' line from a different diffraction order.

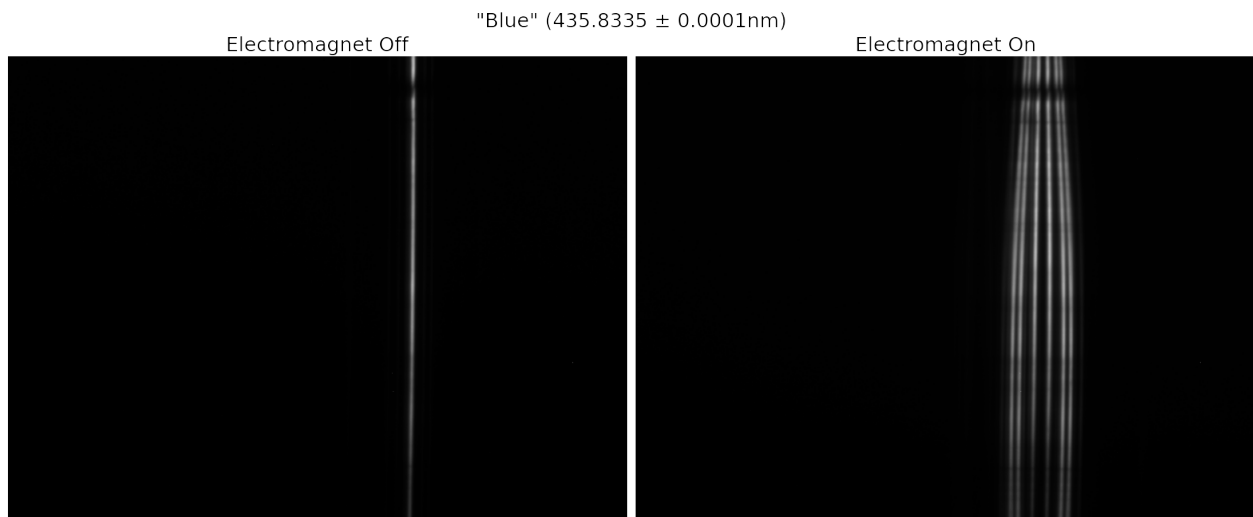


Figure 4.3: Zeeman splitting of the 'blue' line.

Viewing of line splitting may be difficult with images (Fig 4.2). We obtain relative intensity distributions by using the horizontal cross-section with the largest line splitting (which corresponds to where the poles of the electromagnet act) in ImageJ. Greyscale values are all normalized to obtain relative intensity.

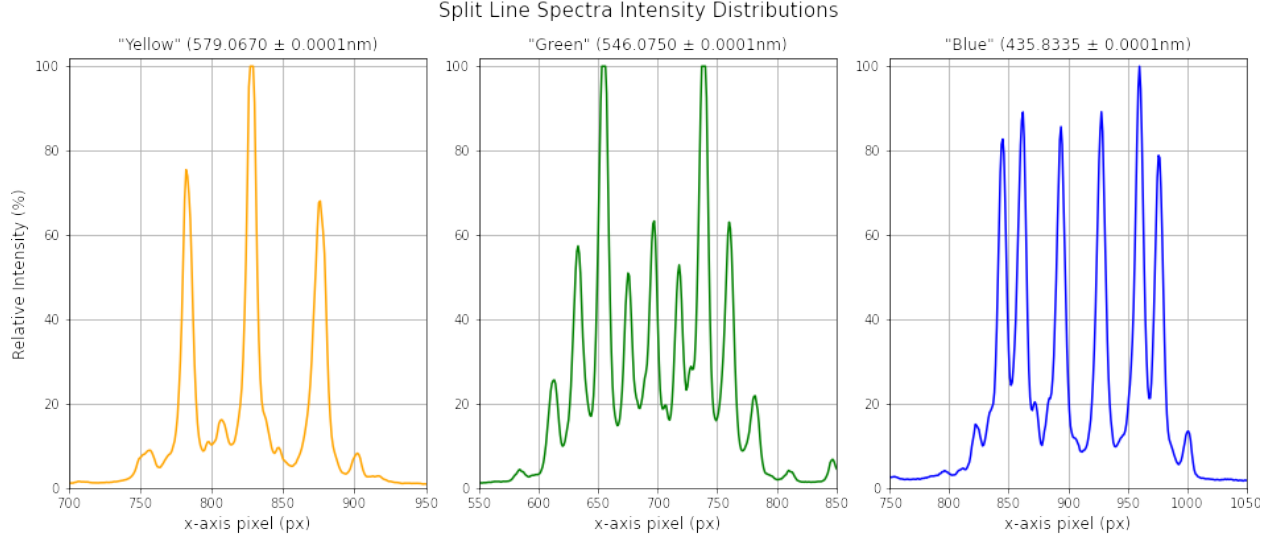


Figure 5: Relative intensity distributions of line splittings'. Taken from horizontal section of largest spectral width.

Examination of images in Fig 4.1, 4.2 and 4.3 suggest existence of the Zeeman effect. Moreover, the intensity distributions of Fig. 5 show splitting into 3, 9 and 6 spectral lines for the 'yellow', 'green' and 'blue' lines respectively, in agreement with predictions.

There are smaller peaks within the intensity distributions which are visible in Fig 5. These are large enough that they are ruled out as noise fluctuations. Underlying causes may be overlapping lines of other diffraction orders, other mercury isotopes of lower abundance or fine-structure corrections. However the spectrometer does not have enough resolution in order to give a confident judgement.

Measurements of $H\alpha$ lines:

We present the CCD image of the $H\alpha$ lines. To form the relative intensity distributions, we apply the same process but also subtract the average background noise. This is accomplished by subtracting the greyscale average of pixels away from the line spectra peaks. These are found in Fig 6.1 and 6.2.

Fig 6.1 shows observed line spectra. One can clearly see two main lines, one to the left (deuterium) and one to the right (protium). Among each main line, it is faintly visible that it is composed of two spectral lines (evidence of fine structure).

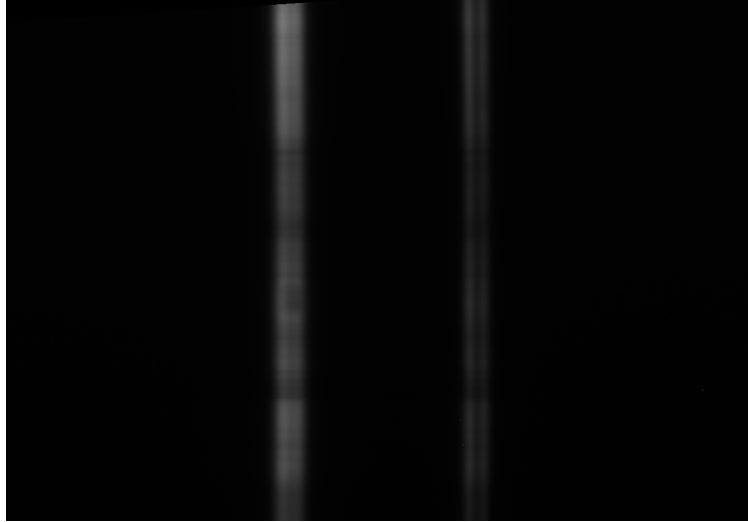


Figure 6.1: Captured $H\alpha$ lines of protium and deuterium.

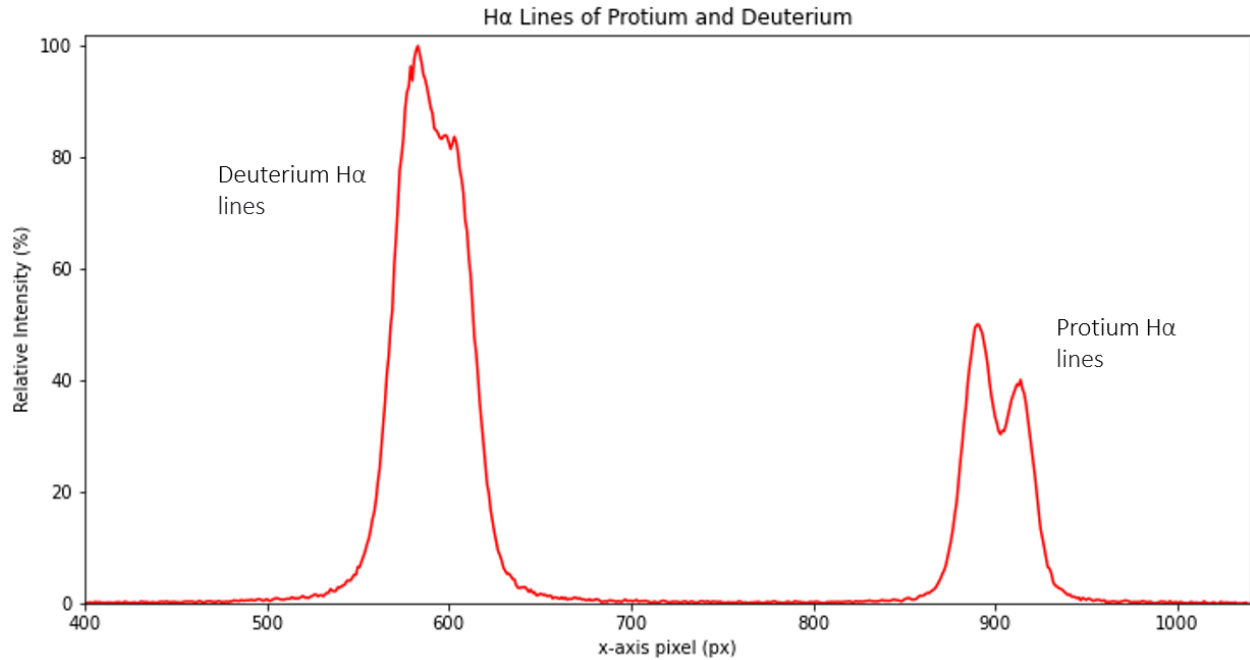


Figure 6.2: Intensity distribution of the measured $H\alpha$ lines of protium-deuterium. (Background noise subtracted)

The intensity distributions of Fig 6.2 show clearer evidence of the fine structure in protium, with two partly distinguished peaks which form the $H\alpha$ line. However for the deuterium $H\alpha$ line, the second peak is completely obscured. Doppler broadening is dominant due to the low mass and high thermal velocity of hydrogen, causing lines to broaden and superimpose with peaks partially or not resolvable[1]. Doppler broadening takes form of a Gaussian distribution, since velocities follow the Maxwell-Boltzmann distribution (which is Gaussian).

To resolve peaks, we perform a curve fitting of the form

$$I(x) = \sum_{i=1}^4 A_i \exp \left[-\frac{(x - x_i)^2}{2\sigma_i^2} \right] \quad (4)$$

which is a superposition of four Gaussians to represent each peak. This is done in Python with the SciPy ‘curvefit’ function, which performs regression using minimization of chi-squared.

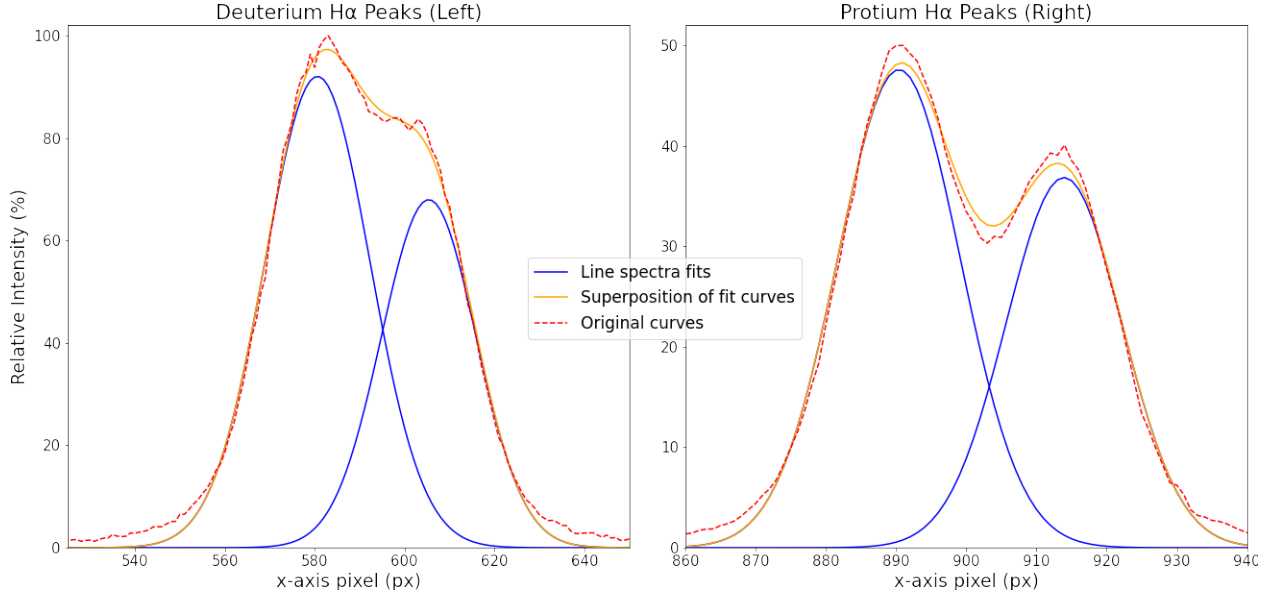


Figure 7: Fitted Gaussian curves to protium-deuterium line spectra.

Note fits in Fig. 7 are not completely satisfactory with tails of the distribution underestimated. This is because although doppler broadening is dominant, there exists other smaller broadening mechanisms such as pressure broadening. The true distribution is given by a ‘Voight profile’ which is a convolution of Gaussian and Lorentzian curves [12]. For our purpose of finding peaks, the Gaussian is sufficient.

We make identifications that larger peaks (${}^2P_{3/2}$) correspond to the same quantum transition and likewise for smaller peaks (${}^2P_{1/2}$) [4]. This is because nuclei mass should not significantly impact the relative transition probabilities of any two transitions. We take peak values of the fitted curves to find peak widths, with uncertainty equal to the standard deviations of the fit. Two calculations of wavelength width are found. Uncertainties are propagated through Eq. 2 and 3.

$(3s) \ ^2S_{1/2} \rightarrow$	$(2p) \ ^2P_{1/2}$	$(2p) \ ^2P_{3/2}$
λ_P (nm)	656.456	656.472
Δx	310 ± 14	308 ± 13
$\lambda_P - \lambda_D$ (nm)	0.176 ± 0.008	0.177 ± 0.008
M_P/M_D (raw value)	0.5069 ± 0.0213	0.5047 ± 0.0233

Table 2: Measured pixel-width(Δx) and calculated values from Eq.2 and 3. λ_P is obtained from NIST [10]. Pixel, wavelength widths are rounded.

Averaging the mass ratios found in Table 2. and propagating error gives the final rounded result of 0.51 ± 0.02 . This is in agreement with the accepted value of 0.5002 [5].

4 Conclusions, Improvement

Overall we find results consistent with predictions produced by quantum physics. Perturbation theory accurately predicts the number of line splittings in neutral mercury atoms, we obtain a proton-deuteron mass ratio in agreement with and under 2% error of the accepted value.

The main limitation of this experiment is principally from doppler broadening of spectral lines. This reduces resolution of spectral lines, hiding subtler physical properties such as fine structure. Provided the resolution of the spectrometer increases, doppler broadening will negate this change, therefore forming an upper limit for the resolution power of the spectrometer.

Due to the nature of doppler broadening, its elimination is somewhat non-trivial. We may remove broadening by reducing the emission source to low temperatures thereby removing thermal velocity of atoms. This can be achieved with doppler cooling, in very simple terms using laser frequencies to induce photon emission in atoms, removing their momentum. This may be implemented with a magneto-optical-trap (MOT), but such configuration is substantially more sophisticated than the current apparatus and is not practical [3]. But if one can reduce doppler broadening, precision of the experiment substantially improves.

A second improvable limitation is the elimination of random noise. Elimination of noise may allow smaller properties which were previously scrambled by noise to be visible. This is attainable by increasing line spectra intensity so noise is relatively smaller or reducing the noise itself. Increasing spectra intensity can be obtained by modifying apparatus. One may use focusing and collimating lenses to collect and focus light from the source into the spectrometer with greater intensity. We

may also eliminate noise through data analysis, using noise-processing algorithms. The Golay-Savitsky filter appears especially useful in spectroscopy since it applies analytically for equally spaced datapoints and averages out random noise by using repeated polynomial fits [11]. When applied on our dataset, there was insignificant change (hence omitted) but may become important when spectrometer resolution is improved.

References

- [1] A. L. Schawlow, "*Lasers, light, and matter*", J. Opt. Soc. Am. 67, pp 140-147 (1977) Available at: <https://opg.optica.org/josa/abstract.cfm?uri=josa-67-2-140>
- [2] Bransden, Brian H, and Charles J Joachain. "*Physics of Atoms and Molecules*", Harlow ; Munich, Prentice Hall, 2010, pp. 215–219.
- [3] Chen, Liang, et al. "*Planar-Integrated Magneto-Optical Trap*", Arxiv, 16 July 2021. Available at: <https://arxiv.org/pdf/2107.07367.pdf>
- [4] Churchill, Chris . *Atomic Transitions*. New Mexico State University, pp. 47 – 67, 15 Feb. 2010. Available at: <http://astronomy.nmsu.edu/cwc/Teaching/ASTR605/Lectures/atomicphys.pdf>
- [5] "*CODATA Value: Deuteron-Proton Mass Ratio.*", NIST, Physics.nist.gov, 2018, Available at: <https://physics.nist.gov/cgi-bin/cuu/Value?mdsmp>
- [6] D. R. Austin, T. Witting, and I. A. Walmsley, "*Broadband astigmatism-free Czerny-Turner imaging spectrometer using spherical mirrors*", Applied Optics, vol. 48, no. 19, p. 15, Jun. 2009, doi: <https://doi.org/10.1364/ao.48.003846>
- [7] E. B. Saloman, "*Wavelengths, Energy Level Classifications, and Energy Levels for the Spectrum of Neutral Mercury*", Journal of Physical and Chemical Reference Data, vol. 35, no. 4, p. 11, Dec. 2006, doi: <https://doi.org/10.1063/1.2204960>
- [8] F. C. Jahoda, F. L. Ribe, and G. A. Sawyer, "*Zeeman-Effect Magnetic Field Measurement of a High-Temperature Plasma*", Physical Review, vol. 131, no. 1, pp. 24–29, Jul. 1963, doi: <https://doi.org/10.1103/physrev.131.24>.
- [9] Khundkar, Lutfur R. "*Mass Ratio of the Deuteron and Proton from the Balmer Spectrum of Hydrogen: Variation on an Undergraduate Physical Chemistry Experiment*", Journal of Chemical Education, vol.73, no. 11, Nov. 1996, p.1055, <https://doi.org/10.1021/ed073p1055>

- [10] NIST. “*Energy Levels of Hydrogen and Deuterium.*” NIST, 21 July 2009, Available at: www.nist.gov/pml/energy-levels-hydrogen-and-deuterium.
- [11] R. Schafer, “*What Is a Savitzky-Golay Filter? [Lecture Notes]*,” IEEE Signal Processing Magazine, vol. 28, no. 4, pp. 111–117, Jul. 2011, doi: <https://doi.org/10.1109/msp.2011.941097>
- [12] Schreier, F. “*The Voigt and Complex Error Function: A Comparison of Computational Methods.*” Journal of Quantitative Spectroscopy and Radiative Transfer, vol. 48, no. 5-6, Nov. 1992, pp. 743–762, [https://doi.org/10.1016/0022-4073\(92\)90139-u](https://doi.org/10.1016/0022-4073(92)90139-u). Available at: <https://lweb.cfa.harvard.edu/~kchance/EPS238-2014/refdata/schreier-voigt-jqsrt-1992.pdf>
- [13] S. Maungkorn and W. Kriwattanawong “*A study of star formation by $H\alpha$ emission of galaxies in the galaxy group NGC 4213*” 2017 J. Phys.: Conf. Ser. 901 012004 Available at: <https://iopscience.iop.org/article/10.1088/1742-6596/901/1/012004/pdf>.

Appendix A

To obtain the result of Eq. 2, we start by noting we can write the energy levels of the single electron atoms with the following form

$$E_n = -\frac{hcR_\infty}{n^2} \left(\frac{M_N}{M_N + m_e} \right) \quad (5.1)$$

Where M_N is the mass of the nucleus, m_e the electron mass. R_∞ is the Rydberg constant. Its value will not be used. n is the principal quantum number. Using Eq. 5.1 we may write the emission transition wavelengths of protium and deuterium in terms of initial state and final state principal quantum numbers, n_i and n_f .

$$\frac{1}{\lambda_P} = \frac{E_i - E_f}{hc} = R_\infty \left(\frac{M_P}{M_P + m_e} \right) \left[\frac{1}{n_f^2} - \frac{1}{n_i^2} \right] \quad (5.2)$$

$$\frac{1}{\lambda_D} = \frac{E_i - E_f}{hc} = R_\infty \left(\frac{M_D}{M_D + m_e} \right) \left[\frac{1}{n_f^2} - \frac{1}{n_i^2} \right] \quad (5.3)$$

For the $H\alpha$ spectral line, n_i and n_f are the same for both protium and deuterium. Dividing Eq. 5.2 by 5.3 gives

$$\frac{\lambda_D}{\lambda_P} = \frac{M_P(M_D + m_e)}{M_D(M_P + m_e)} \quad (5.4)$$

Then using Eq. 5.4, it is easy to compute

$$\frac{\Delta\lambda}{\lambda_P} = \frac{\lambda_P - \lambda_D}{\lambda_P} = 1 - \frac{\lambda_D}{\lambda_P} \quad (*)$$

$$\frac{\Delta\lambda}{\lambda_P} = 1 - \frac{M_P(M_D + m_e)}{M_D(M_P + m_e)} = \left(1 - \frac{M_P}{M_D} \right) \left(1 + \frac{M_P}{m_e} \right)^{-1} \quad (5.5)$$

Careful rearrangement of Eq. 5.5 gives

$$\frac{M_P}{M_D} = 1 - \left(1 + \frac{M_P}{m_e} \right) \frac{\Delta\lambda}{\lambda_P} \quad (5.6)$$

This is the same as Eq. 2 with $\Delta\lambda = \lambda_P - \lambda_D$. Note here we have ignored the fine-structure energy corrections. Eq. 5.6 therefore serves as a form of approximation, however considering the precision of the spectrometer, fine structure can be easily neglected and the equation can be taken as accurate.

Appendix B

Echelle diffraction gratings are characterized by large blaze angles. As a result, we may consider the figure below:

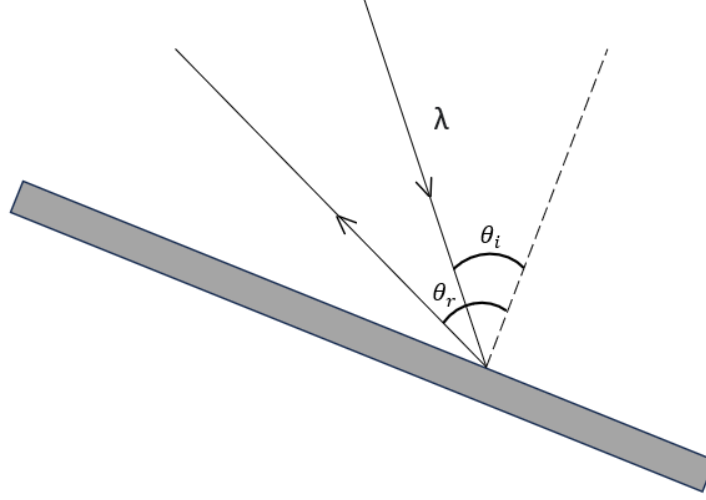


Figure 8. Light diffracted off of an echelle grating.

A relation between the incident angle (θ_i) and reflected angle (θ_r) of light is related to the wavelength by the diffraction equation, namely

$$\sin \theta_i + \sin \theta_r = \frac{m\lambda}{d} \quad (6.1)$$

Where d is the grating spacing, m is the order. Assuming incident angle of light is kept constant, differentiation with respect to θ_r gives

$$\frac{d\theta_r}{d\lambda} = \frac{m}{d \cos \theta_r} \quad (6.2)$$

Using Eq. 6.1, we substitute the value of m/d with λ , θ_i and θ_r

$$\frac{d\theta_r}{d\lambda} = \frac{\sin \theta_i + \sin \theta_r}{\lambda \cos \theta_r} \quad (6.3)$$

A horizontal change in position is related to the change in angle by

$$\frac{dx}{d\theta_r} = f \quad (6.4)$$

Where f is the focal length of the collimating mirror, since our output should be focused images. By chain rule (Eq. 6.3 and 6.4),

$$\frac{dx}{d\lambda} = f \left[\frac{\sin \theta_i + \sin \theta_r}{\cos \theta_r} \right] \frac{1}{\lambda} = \frac{7418}{\lambda} \quad (mm/nm) \quad (6.5)$$

Where we have used $f = 1600mm$ and $\theta_i = 63^\circ$, $\theta_r = 67^\circ$ which characterize the blaze angle values (we assume uncertainty is negligible in these values). By measuring λ in units of nm, we obtain an expression with dimensions mm/nm.

We convert this into a CCD pixel width. By noting the CCD camera has a pixel width of $6.45\mu m$ (assume negligible uncertainty), we obtain

$$\frac{dx}{d\lambda} = \frac{1.150 \times 10^6}{\lambda} \quad (6.6)$$

Which has units pixels/nm. We show that this leads to the first-order-approximation:

$$\Delta\lambda \approx \frac{\lambda_P}{1.150 \times 10^6} \Delta x \quad (6.7)$$

which is precisely Eq. 3. Suppose we want to find the pixel width between the two wavelengths λ_P and λ_D . By integration of Eq. 6.6, this gives

$$\frac{\Delta x}{1.150 \times 10^6} = \ln \left(\frac{\lambda_P}{\lambda_D} \right) = \ln \left(1 + \frac{\Delta\lambda}{\lambda_D} \right) \quad \Delta\lambda = \lambda_P - \lambda_D \quad (6.8)$$

Since $\Delta\lambda$ is sufficiently small relative to λ_D , we perform a Taylor expansion

$$\frac{\Delta x}{1.150 \times 10^6} = \frac{\Delta\lambda}{\lambda_D} - \frac{1}{2} \left(\frac{\Delta\lambda}{\lambda_D} \right)^2 + \dots \quad (6.9)$$

Notice, in Eq. 6.7 we have λ_P . We rewrite the first term on the RHS as

$$\frac{\Delta x}{1.150 \times 10^6} = \frac{\Delta\lambda}{\lambda_P} \left[1 - \frac{\Delta\lambda}{\lambda_P} \right]^{-1} - \frac{1}{2} \left(\frac{\Delta\lambda}{\lambda_D} \right)^2 + \dots \quad (6.10)$$

Since $\Delta\lambda$ is sufficiently small relative to λ_P , we perform another Taylor expansion. Expanding brackets and multiplying by λ_P , we find

$$\frac{\lambda_P}{1.150 \times 10^6} \Delta x = \Delta\lambda + \left[\frac{(\Delta\lambda)^2}{\lambda_P} - \frac{1}{2} \frac{(\Delta\lambda)^2 \lambda_P}{\lambda_D^2} + \dots \right] \quad (6.11)$$

The order of error is dominated by quadratic terms in the brackets. Since λ_P , $\lambda_D \approx 650$, $\Delta\lambda \approx 0.1$, this yields a calculation of roughly 10^{-5} nm. This is much more precise than the spectrometer hence it is valid to drop the bracketed terms, yielding Eq. 3.